How to cite: *Angew. Chem. Int. Ed.* **2022,** *61,* e202117058
International Edition: doi.org/10.1002/anie.202117058
German Edition: doi.org/10.1002/ange.202117058

CO_2 Reduction Hot Paper

Assembling Metal Organic Layer Composites for High-Performance Electrocatalytic CO_2 Reduction to Formate

Hang Liu, Hongguang Wang,* Qian Song, Kathrin Küster, Ulrich Starke, Peter A. van Aken, and Elias Klemm**

Abstract: *2D metal–organic-framework (MOF) based composites have emerged as promising candidates for electrocatalysis due to their high structural flexibility and fully exposed active sites. Herein, a freestanding metal–organic layer (MOL) with a 2D kgd (kagome dual) lattice was constructed with abundant surface oxygenate groups serving as anchoring sites to immobilize diverse guests. Taking Bi as an example, tetragonal Bi_2O_3 nanowires can be uniformly grown on MOLs after solvothermal treatment, the structural evolution of which was followed by ex situ electron microscopy. The as-prepared Bi_2O_3/MOL exhibits excellent CO_2 electroreduction activity towards formate reaching a specific current of 2.3 A mg_{Bi}^{-1} and Faradaic efficiencies of over 85 % with a wide potential range from −0.87 to −1.17 V, far surpassing Bi_2O_3/UiO (a 3D Zr_6-oxo based MOF) and Bi_2O_3/AB (Acetylene Black). Such a post-synthetic modification strategy can be flexibly extended to develop versatile MOL composites, highlighting the superiority of optimizing MOL-based composites for electrocatalysis.*

Introduction

Electrocatalytic CO_2 reduction (ECR) to fuels (such as formic acid/formate) is regarded as a promising strategy to alleviate energy and environmental dilemmas, especially considering the recent progress in competitive renewable electricity.[1] In particular, formic acid/formate is of high value in the chemical market and can also serve as a hydrogen carrier for fuel cells, making it an attractive CO_2 reduction product.[2] Early researches of bulk metals (such as Sn, In, Bi, Pb, Co) as working electrodes failed to achieve satisfactory performance, with respect to durability, activity, selectivity and cost, highlighting the significance of developing novel catalysts.[3,4] Among them, Bi-based catalytic sites, even though a late start, are receiving much attention, due to their superiority on selectivity towards formic acid/formate.[4]

Metal–organic frameworks (MOFs), constructed by metal-based secondary building units (SBUs) and organic bridging ligands to form 3D rigid frameworks, have attracted extensive interest as versatile platforms for diverse research fields, especially in catalysis.[5a] Featuring ultra-high surface areas, versatile porosities, flexible structures, and high crystallinities, MOFs are promising candidates for superior activities and investigating the structure–activity relationship.[5] However, the electrically insulating nature of most pristine MOFs hinders effective electron transfer to the inner surface, disabling a large proportion of the active sites.[6] Constructing metal–organic layers (MOLs) instead of 3D-MOFs possessing fully exposed active surfaces, could be a promising strategy to enable electrocatalysis in MOFs without abandoning structural flexibility.[7] Moreover, abundant surface groups from either metal SBUs or ligands open up the possibility of post-synthetic modifications.[8] Optimizing post-synthetic modification strategies to construct novel and high-performance MOL composites for ECR is promising and predictable, but not well investigated yet.[9]

Herein, we synthesize a freestanding MOL with *kgd* (kagome dual) lattice of monolayer thickness by a one-pot bottom-up synthesis. The Zr_6–oxo clusters as building blocks ensure the high stability and flexibility to load active sites through abundant surface anchoring sites. Taking Bi, a well-known active site for CO_2 reduction, as a representative, tetragonal Bi_2O_3 nanowires can be uniformly dispersed on MOLs. The structural evolution starting from atomic modification of the Bi sites, growing to nanoscale wires, was monitored by ex situ transmission electron microscopy (TEM) and high-angle annular dark-field scanning transmission electron microscopy (HAADF-STEM). The novel Bi_2O_3/MOL showed excellent ECR performance, exhibiting a maximum formate current density of 2.3 A mg_{Bi}^{-1} and Faradaic efficiencies (FEs) of over 85 % under a wide voltage range from −0.87 to −1.17 V, compared with Bi_2O_3 loaded onto a 3D MOF (Bi_2O_3/UiO) or on the acetylene black substrate (Bi_2O_3/AB). The performance maintains over 21 h at −0.97 V, indicating the durable catalytic stability of Bi_2O_3/MOL. Furthermore, by integrating the Bi_2O_3/MOL into a gas diffusion electrode, technically relevant current densities of 300 mA cm^{-2} can be reached

[*] H. Liu, Dr. Q. Song, Prof. E. Klemm
Universität Stuttgart
Institut für Technische Chemie
Pfaffenwaldring 55, 70569 Stuttgart (Germany)
E-mail: hang.liu@itc.uni-stuttgart.de
elias.klemm@itc.uni-stuttgart.de
Dr. H. Wang, Dr. K. Küster, Prof. U. Starke, Dr. P. A. van Aken
Max Planck Institute for Solid State Research
Heisenbergstraße 1, 70569 Stuttgart (Germany)
E-mail: hgwang@fkf.mpg.de

keeping the Faradaic efficiencies above 80%. This post-synthetic modification on MOLs can be extended to other guests, underscoring the adjustability and superiority of exploring MOL composites for high-performance electrocatalysis.

Results and Discussion

Synthesis and Characterizations of Zr-TATB MOL

Zr_6–oxo clusters are widely adopted in the construction of MOFs, owing to their outstanding chemical stability and high tunability.[10] We synthesized Zr-TATB MOL by a facile solvothermal reaction of $ZrOCl_2 \cdot 8H_2O$ and a tridentate linker (4,4′,4″-*s*-triazine-2,4,6-triyl-tribenzoate linker, H_3TATB), which has not yet been reported for MOL constructions, in an acetic acid (HOAc)/N,N-dimethylformamide (DMF) mixture. According to pioneering works of MOLs, 6-connected Zr_6–oxo clusters and 3-connected TATBs are expected to be coordinated with each other with the assistance of capping modulators (HOAc), to obtain a rigid 2D-*kgd* topology (Figure 1a, Supporting Information, Figure S1).[11] Scanning electron microscopy (SEM) images show a layered structure without large bulk particles (Figure S2). The layered structure can also be verified by the N_2 adsorption test, giving a type II isotherm plot, corresponding to non-porous materials (Figure S3). Thermogravimetric analysis (TGA) indicates that the MOL decomposes above 400 °C in the air (Figure S4), suggesting a good thermal stability. Chemical stability was also demonstrated by soaking in a common electrolyte overnight, followed by powder X-ray diffraction (PXRD) tests (Figure S5).

In the absence of single crystals, we applied multiple characterization techniques to determine detailed structural information. The PXRD pattern of the Zr-TATB MOL matches well with the simulated crystal structure with a preferred orientation of (001) (Figure 1b, S6), ruling out other possible 3D structures (Figure S7, S8). Proton nuclear magnetic resonance spectroscopy (^{1}H NMR) of the dissolved Zr-TATB MOL confirmed the presence of acetate and TATB ligand with a ratio of 2.8:1, close to the theoretical value of 3:1 (Figure 1c, S9).[12] The ratio of Zr:TATB as determined by TGA is 3:1 (Figure S4), which fits well with the proposed structure. Aberration-corrected TEM has been employed to image the lattice structure of the MOL. The obtained TEM image, the corresponding fast Fourier transform (FFT) pattern, and the selected area electron diffraction (SAED) pattern confirmed the hexagonal symmetry of the layer, matching the 2D *kgd* lattice (Figure 1d, S10, S11). By high-resolution transmission electron microscopy (HRTEM) and STEM, the Zr_6-oxo clusters appear as black dots arranged with hexagonal symmetry (Figure 1e, S12). The distance between adjacent clusters is 1.94 nm, very close to that of the simulated MOL structure (1.95 nm). Additionally, atomic force microscopy (AFM) images of the Zr-TATB MOL gave an average thickness of 1.48 nm (Figure 1f, S13), compatible with the van der Waals size of the Zr-TATB monolayer. It is somewhat thicker than

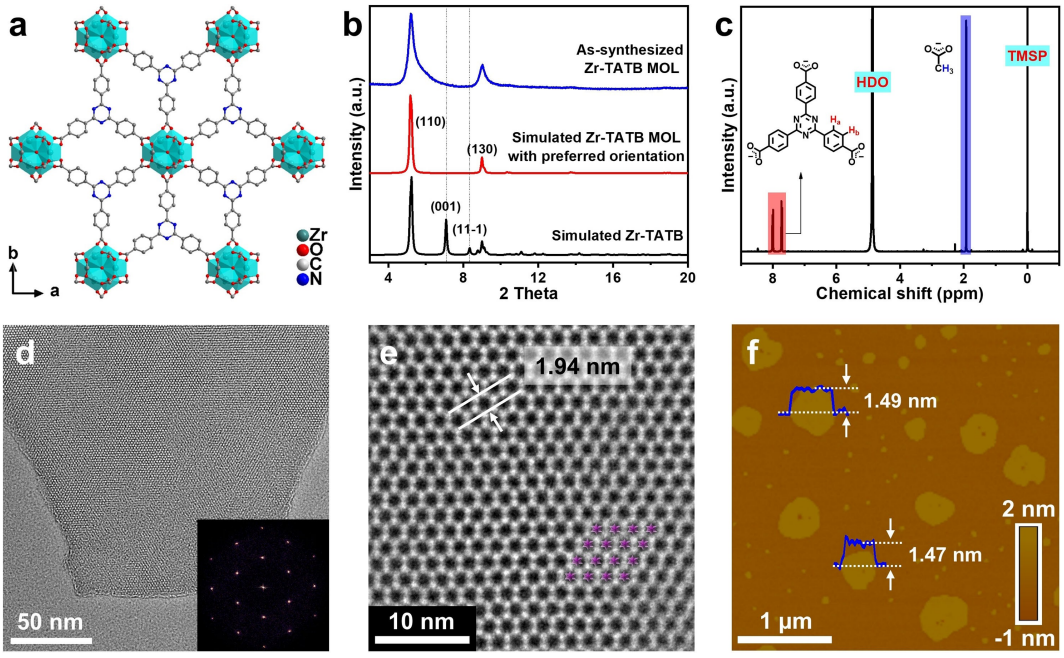

Figure 1. a) Scheme illustrating the structure of the Zr-TATB MOL with *kgd* topology viewed from *c* axis. b) PXRD patterns of the simulated structure with/without preferred (001) orientation and as-synthesized Zr-TATB MOL. c) ^{1}H NMR spectrum of the dissolved Zr-TATB MOL, using *d4*-trimethylsilylpropanoic acid (*d4*-TMSP) sodium salt of known concentration as the internal standard. d) TEM and e) HRTEM images of the Zr-TATB MOL, acquired with the total electron dose of 1.0×10^4 $e^- nm^{-2}$ (inserted: FFT pattern). f) AFM analysis with height profiles (blue) of the Zr-TATB MOL to determine the thickness.

the isoreticular Zr-BTB,[11b] due to acetate being larger than hydroxyl (Figure 1c). These data confirm the successful direct synthesis of the Zr-TATB monolayer.

The external surface of Zr-TATB MOL is fully accessible and contains abundant sites for facile post-synthetic modifications, making it an ideal platform for designing diverse electrocatalysts. In general, six carboxylate groups coordinate to the Zr_6–oxo cluster presenting a planar hexagonal symmetry, while leaving six paired $–OH_x$ or capping modulators (acetate in Zr-TATB MOL) vertically oriented (Figure S14a). The binding of acetate as a capping agent is flexible and can be exchanged by –OH to provide ample anchoring sites (Figure S14b).[8a] Based on this principle, certain reports have achieved the loading of single-atom or ultrafine clusters on similar systems.[8] However, further steps to develop uniform nanoparticles decorated MOL composites are still rarely reported, which is of high interest for expanding the universality of MOFs for diverse catalysis.

Synthesis and Characterizations of Bi_2O_3/MOL

Considering the inertness of Zr in the electro-catalytic CO_2 reduction reaction, we decided to load bismuth, which is a classic active site for formate generation, on the MOLs.[4] Generally, Bi loading was conducted by a facile solvothermal reaction of MOL with $Bi(NO_3)_3$ using DMF as a solvent. The Bi loading was 2.61 wt % as determined by inductively coupled plasma atomic emission spectroscopy (ICP-AES) (Table S1). HAADF-STEM showed the morphology and location of the guest Bi compound. The bright nanowires with an average diameter of 6 nm in STEM dark-field images could be identified as a Bi compound, which was uniformly distributed on the MOL (Figure 2a, b, S15). Further electron energy-loss spectroscopy (EELS) maps unambiguously corroborated the distribution of Bi and Zr (Figure 2b), whereby Bi was mainly concentrated on the nanowires on Zr_6–oxo based MOL. A high-resolution STEM image presented a clear lattice pattern of nanowires (Figure 2c), indicating the good crystallinity of the guest Bi compound. Such a modification is rather mild without damaging the crystal structure of the MOL, verified by the retention of diffraction peaks in PXRD patterns (Figure 2d). A rather broad diffraction peak centered at 28° can also be assigned to tetragonal β-Bi_2O_3, as the best matching (hereafter denoted as Bi_2O_3/MOL). The successful formation of such tiny Bi_2O_3 by MOLs avoids the generally adopted capping agents and verifies the structural advance of constructing MOL composites.

Besides Bi_2O_3 nanowires, ultrafine Bi dots can also be observed in the HAADF-STEM (Figure S15). To determine another Bi state, a control sample (denoted as BiO_x/MOL) was synthesized at room temperature, corresponding to the primary stage of Bi_2O_3/MOL synthesis with suppressed hydrolysis/agglomeration. The PXRD pattern gave only the diffraction from Zr-TATB MOL (Figure S16), implying the disappearance of the crystalline Bi_2O_3 nanoparticles. This is supported by high-resolution STEM images, which show only a few heterogeneous nanoparticles (Figure S17). Further EELS mappings confirm the presence of Bi on MOL with even dispersion (Figure 2e). Such ultra-high dispersion can be speculated as sub-nanometer dominated BiO_x through ion modification (Figure S14).[8a] X-ray photoelec-

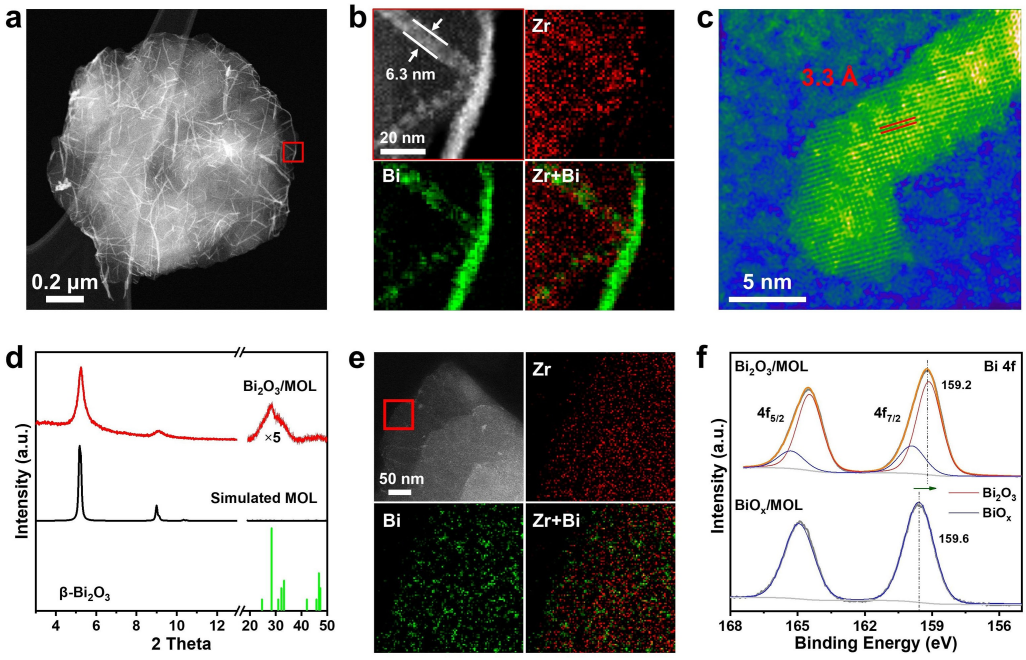

Figure 2. a) HAADF-STEM overview image, b) EELS mapping and c) high-resolution STEM image of the Bi_2O_3/MOL. d) PXRD patterns of standard β-Bi_2O_3, simulated Zr-TATB MOL with (001) preferred orientation, and as-synthesized Bi_2O_3/MOL. e) HAADF-STEM image with EELS mapping of BiO_x/MOL (The mapping area is marked by a red square). f) Bi 4f XPS spectra of Bi_2O_3/MOL and BiO_x/MOL.

tron spectra (XPS) of BiO_x/MOL give an apparently higher binding energy (159.6 eV) than Bi_2O_3/MOL (159.2 eV) (Figure 2f), the latter of which is dominated by crystalline Bi_2O_3. The feature at higher binding energy can be ascribed to a more oxidized Bi state, consistent with oxygen-rich non-crystalline BiO_x. Therefore, the Bi 4f signals of Bi_2O_3/MOL can be fitted as two components of trivalent Bi, 76.3 % β-Bi_2O_3 (159.1 eV) and 23.7 % BiO_x (159.9 eV) (Figure 2f, Table S2).[13]

The transformation of BiO_x/MOL into Bi_2O_3/MOL inspired us to investigate the mechanism of the formation of MOL composites more thoroughly. The formation of Bi species was followed using ex situ electron microscopy studies by sampling at different synthesis times (Figure S18). Bi was loaded with ultra-high dispersion and a few non-crystalline particles formation, prior to hydrothermal treatment (Figure S16, S17). This phenomenon can be ascribed to fast ion immobilization by multiple surface anchoring sites.[8a] The reversible coordination of Bi ions to Zr_6-oxo clusters makes further rearrangement possible, promoted by the solvothermal treatment. Adjacent Bi sites aggregate into clusters, serving as seeds for the subsequent growth (Figure 3). Over the total reaction time, small nanoparticles gradually grew into nanowires on the MOL (Figure S18). The loading gradually increased with time, reaching a maximum after around 12 hours (Figure S19).

Evaluation of Electrocatalytic CO_2 Reduction

To underline the superiority of MOL based composites, a typical 3D-MOF (Zr_6-oxo SBUs based MOF, known as UiO-66) and acetylene black (denoted as AB), as references, were both loaded with Bi by the same method to obtain Bi_2O_3/UiO and Bi_2O_3/AB, respectively. From PXRD of Bi_2O_3/UiO, a broad peak at around 28° indicated the formation of β-Bi_2O_3 (Figure S20). The comparison of TEM images with bare UiO-66 suggested the formation of Bi_2O_3 nanowires in UiO-66 (Figure S21). Based on its XPS spectrum (Figure S18), UiO-66 is less inclined to the formation of Bi_2O_3 nanowires (61.9 %) than Bi_2O_3/MOL (76.3 %) (Figure S22, Table S2). This can be attributed to the fact that the rearrangement of Bi ions to nanowires is subject to steric hindrance in the inner pores (Figure S23). When applied to the typical conductive support (AB), Bi_2O_3 is mainly in the form of nanoparticles (≈3 nm), interspersed with few nanowires, as characterized by PXRD, HAADF-STEM, EELS mapping and XPS (Figure S24–S27). The reduced percentage of Bi_2O_3 nanowires may be due to the lack of dense anchoring sites, emphasizing the template effect of MOLs.

For ECR reactions, working electrodes were prepared by drop-casting onto carbon paper (CP) with ink containing catalysts and AB, and tested in a typical H-type cell using 0.5 M $KHCO_3$ as electrolyte (Scheme S1). The AB as a conductive additive was added to increase the electrical contact between the electrocatalyst and CP, and to prevent the stacking of MOL composites, giving an overall activity enhancement (Figure S28, S29). Bare Zr-TATB MOL exhibited a much lower current response and gave only hydrogen evolution, which is not surprising because bare MOLs are free of active sites for ECR (Figure S30). As revealed by linear sweep voltammetry (LSV) curves, Bi_2O_3/MOL presented the largest current response under CO_2 and the most significant difference between Ar/CO_2 compared to other references (Figure 4a), implying higher activity towards ECR. Faradaic efficiencies of the Bi_2O_3 based catalysts were further investigated by chrono-amperometry at different applied potentials. Bi_2O_3/MOL maintains superior formate selectivities of over 85 % over a wide potential range from −0.87 V to −1.17 V vs. RHE (reversible hydro-

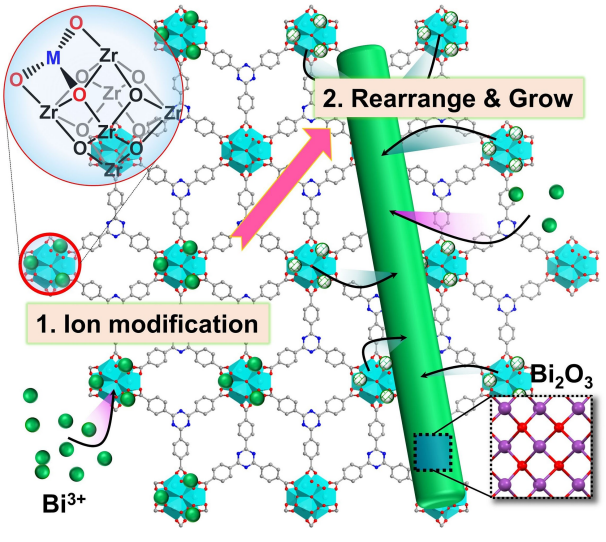

Figure 3. Scheme illustrating the post-synthetic modification strategy to construct Bi_2O_3/MOL composites. Two steps are proposed: 1. Bi^{3+} ion modification by multiple oxygenated groups (–OH_x) on the MOL. 2. The immobilized Bi sites were rearranged and grown into Bi_2O_3 nanowires.

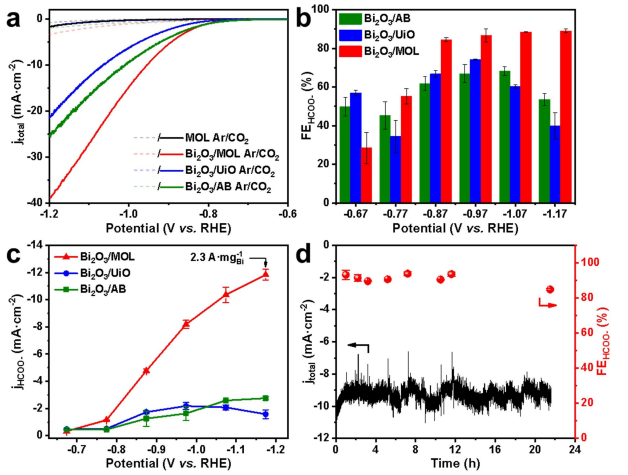

Figure 4. a) LSV curves under Ar/CO_2, b) Faradaic efficiencies and c) current densities of ECR to formate at different potentials over Bi_2O_3/MOL, Bi_2O_3/UiO and Bi_2O_3/AB. d) Durability test of Bi_2O_3/MOL at −0.97 V vs. RHE.

gen electrode) (Figure 4b, S31). H_2 and CO were the main by-products in the absence of other carbonaceous products, determined by gas chromatography (GC) and ^{1}H NMR (Figure S32, S33a). In contrast, Bi_2O_3/UiO and Bi_2O_3/AB only gave maximum FEs of 74 % and 67 %, respectively. The superior performance of Bi_2O_3/MOL is also reflected in the partial current density, based on both the geometry area and mass of Bi (Figure 4c, S33b). The long-term test at −0.97 V gave a good retention of current density and FE over 21 hours (Figure 4d), indicating the stability of the active sites. The structural and chemical stability of MOL and nanowires could be verified by PXRD, TEM and XPS after the reaction (Figure S34–S36, Table S2).

More comparative experiments were conducted to understand the superior performance of Bi_2O_3/MOL. The ECR tests of BiO_x/MOL give an insight into the effect of morphology and crystallinity of the Bi species (Figure S37–S39). To eliminate the influence of the loading effect, ECR tests with composites possessing controlled Bi loadings were supplemented (Figure S40, S41), confirming the superior ECR performance of Bi_2O_3/MOL. Further enhancement of the current density towards industrial requirement can be achieved by gas diffusion electrodes (GDEs), giving a remarkable geometrical formate current density of 330 mA cm^{-2} (Figure S42). To the best of our knowledge, this is the first example to achieve an industrially relevant ECR formate production by MOFs based materials. Overall, Bi_2O_3/MOL exhibits one of the highest performances amongst MOFs used for direct ECR, highlighting the superiority of optimizing MOL composites (Table S3).

The superior activity by MOL composites can be ascribed to the fully exposed surface area for guest immobilization and electrocatalysis. Firstly, a considerable amount of Bi sites is buried within the insulating UiO-66 and thereby prevented from contacting the current collector. This can be verified by oxidative LSV ($Bi^0 \rightarrow Bi^{3+}$) plots that Bi_2O_3/UiO presented a smaller electrochemically active area than Bi_2O_3/MOL with similar Bi loading (Figure S43). Secondly, a reduction process occurs during the ECR of Bi_2O_3/MOL, which is confirmed by the XPS comparison of samples before and after reaction (Figure S36).[4] The stabilities of the catalysts after reaction are estimated by the electrochemically active area of oxidative LSV plots (Figure S44). Bi_2O_3/UiO significantly degraded at electrochemically active sites after electrocatalysis, while Bi_2O_3/MOL exhibited nearly no change. The degraded performance of Bi_2O_3/UiO at more negative potentials (< −1.0 V) may be related to Bi agglomeration on the limited external surface area of UiO (Figure 4b,c), leading to a loss of active sites.

Universality of Constructing MOL Composites

Using MOLs to construct active composites is not limited to Bi but is highly universal. Implementation of other active metals, such as In or Sn, is also possible through our facile post-synthetic modification strategy (Figure 5a,b; Section S5; Figure S45–S49). Additionally, the Bi speciation can be further tailored by slight modifications, giving MOL loaded metallic Bi or BiOCl, as desired (Figure 5c,d; Section S6; Figure S50–S53). Diverse guest compounds can be evenly dispersed onto Zr-TATB MOL and characterized by TEM and PXRD. Moreover, all of them exhibit good ECR performance towards formate (Figure 5; Table S3), illustrating the advantages of constructing MOL composites.

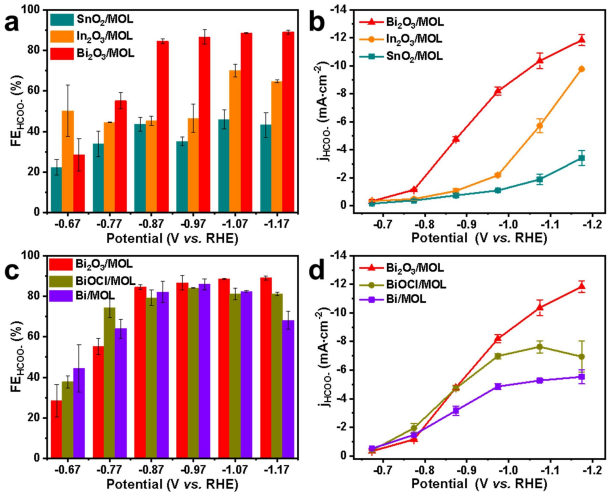

Figure 5. Faradaic efficiencies and current densities of ECR to formate at different potentials over a, b) MOLs loaded with different active metal sites (Bi, Sn and In) and c, d) MOLs loaded with different Bi species (Bi_2O_3, BiOCl and metallic Bi).

Conclusion

In summary, a freestanding metal–organic layer with 2D *kgd* lattice was synthesized using TATB as a single ligand. Due to its high versatility, ultra-exposed surface area and stability, Zr-TATB MOL was chosen as a promising support to load a diverse array of active sites. Taking Bi_2O_3/MOL as an example, the novel structure and formation pathway were clearly revealed by electron microscopy studies, which highlight the template effect of MOL on the construction of composites. In contrast to 3D-MOF-based composites, Bi_2O_3/MOL possesses excellent ECR activity for formate with FEs exceeding 85 % over a wide range of applied potentials and good stability for more than 21 h. The maximum formate current density could reach up to 2.3 A per mg Bi in the H-type cell and unprecedented 330 mA cm^{-2} using gas diffusion electrode, which is the top performance among MOF-based catalysts achieved to date. This work highlights the importance of exploring 2D MOLs and constructing other MOL-based composites with active sites optimized for CO_2 reduction.

Acknowledgements

H. Liu thanks the China Scholarship Council for their generous grant of a Ph.D. scholarship (No. 201806340105). This work is partially funded through the European Union's

Horizon 2020 research and innovation programme under grant agreement No. 823717—ESTEEM3. We greatly thank Prof. Deven P. Estes for proofreading the manuscript. Open Access funding enabled and organized by Projekt DEAL.

Conflict of Interest

The authors declare no conflict of interest.

Data Availability Statement

The data that support the findings of this study are available from the corresponding author upon reasonable request.

Keywords: 2D Composites · CO_2 · Electroreduction · Electron microscopy · MOFs

[1] a) S. J. Davis, K. Caldeira, H. D. Matthews, *Science* **2010**, *329*, 1330–1333; b) C. Hepburn, E. Adlen, J. Beddington, E. A. Carter, S. Fuss, N. Mac Dowell, J. C. Minx, P. Smith, C. K. Williams, *Nature* **2019**, *575*, 87–97; c) S. Sgouridis, M. Carbajales-Dale, D. Csala, M. Chiesa, U. Bardi, *Nat. Energy* **2019**, *4*, 456–465; d) M. G. Kibria, J. P. Edwards, C. M. Gabardo, C. T. Dinh, A. Seifitokaldani, D. Sinton, E. H. Sargent, *Adv. Mater.* **2019**, *31*, 1807166.

[2] a) X. Ji, K. T. Lee, R. Holden, L. Zhang, J. Zhang, G. A. Botton, M. Couillard, L. F. Nazar, *Nat. Chem.* **2010**, *2*, 286–293; b) D. Mellmann, P. Sponholz, H. Junge, M. Beller, *Chem. Soc. Rev.* **2016**, *45*, 3954–3988.

[3] a) Y. Y. Birdja, E. Pérez-Gallent, M. C. Figueiredo, A. J. Göttle, F. Calle-Vallejo, M. T. M. Koper, *Nat. Energy* **2019**, *4*, 732–745; b) W. Ju, A. Bagger, G. P. Hao, A. S. Varela, I. Sinev, V. Bon, B. Roldan Cuenya, S. Kaskel, J. Rossmeisl, P. Strasser, *Nat. Commun.* **2017**, *8*, 944; c) S. Ren, D. Joulié, D. Salvatore, K. Torbensen, M. Wang, M. Robert, C. P. Berlinguette, *Science* **2019**, *365*, 367–369; d) F. P. García de Arquer, C. T. Dinh, A. Ozden, J. Wicks, C. McCallum, A. R. Kirmani, D. H. Nam, C. Gabardo, A. Seifitokaldani, X. Wang, Y. C. Li, F. Li, J. Edwards, L. J. Richter, S. J. Thorpe, D. Sinton, E. H. Sargent, *Science* **2020**, *367*, 661–666; e) C. Yan, H. Li, Y. Ye, H. Wu, F. Cai, R. Si, J. Xiao, S. Miao, S. Xie, F. Yang, Y. Li, G. Wang, X. Bao, *Energy Environ. Sci.* **2018**, *11*, 1204–1210; f) J. Gu, C.-S. Hsu, L. Bai, H. M. Chen, X. Hu, *Science* **2019**, *364*, 1091–1094; g) S. Gao, Y. Lin, X. C. Jiao, Y. F. Sun, Q. Q. Luo, W. H. Zhang, D. Q. Li, J. L. Yang, Y. Xie, *Nature* **2016**, *529*, 68–71; h) A. Löwe, M. Schmidt, F. Bienen, D. Kopljar, N. Wagner, E. Klemm, *ACS Sustainable Chem. Eng.* **2021**, *9*, 4213–4223; i) W. Ma, S. Xie, X. G. Zhang, F. Sun, J. Kang, Z. Jiang, Q. Zhang, D. Y. Wu, Y. Wang, *Nat. Commun.* **2019**, *10*, 892.

[4] a) Z. Yang, F. E. Oropeza, K. H. L. Zhang, *APL Mater.* **2020**, *8*, 060901; b) Q. Gong, P. Ding, M. Xu, X. Zhu, M. Wang, J. Deng, Q. Ma, N. Han, Y. Zhu, J. Lu, Z. Feng, Y. Li, W. Zhou, Y. Li, *Nat. Commun.* **2019**, *10*, 2807; c) N. Zhang, F. Zheng, B. Huang, Y. Ji, Q. Shao, Y. Li, X. Xiao, X. Huang, *Adv. Mater.* **2020**, *32*, 1906477.

[5] a) H. Furukawa, K. E. Cordova, M. O'Keeffe, O. M. Yaghi, *Science* **2013**, *341*, 1230444; b) R. Freund, S. Canossa, S. M. Cohen, W. Yan, H. Deng, V. Guillerm, M. Eddaoudi, D. G. Madden, D. Fairen-Jimenez, H. Lyu, L. K. Macreadie, Z. Ji, Y. Zhang, B. Wang, F. Haase, C. Wöll, O. Zaremba, J. Andreo, S. Wuttke, C. S. Diercks, *Angew. Chem. Int. Ed.* **2021**, *60*, 23946–23974; *Angew. Chem.* **2021**, *133*, 24142–24173; c) L. Jiao, Y. Wang, H.-L. Jiang, Q. Xu, *Adv. Mater.* **2018**, *30*, 1703663; d) H. Jin, C. Guo, X. Liu, J. Liu, A. Vasileff, Y. Jiao, Y. Zheng, S. Z. Qiao, *Chem. Rev.* **2018**, *118*, 6337–6408.

[6] a) L. Sun, M. G. Campbell, M. Dinca, *Angew. Chem. Int. Ed.* **2016**, *55*, 3566–3579; *Angew. Chem.* **2016**, *128*, 3628–3642; b) Y. Xu, Q. Li, H. Xue, H. Pang, *Coord. Chem. Rev.* **2018**, *376*, 292–318; c) X. F. Lu, Y. Fang, D. Luan, X. W. Lou, *Nano Lett.* **2021**, *21*, 1555–1565; d) M. Yu, R. Dong, X. Feng, *J. Am. Chem. Soc.* **2020**, *142*, 12903–12915; e) M. K. Lee, M. Shokouhimehr, S. Y. Kim, H. W. Jang, *Adv. Energy Mater.* **2021**, *11*, 2003990; f) P. Deng, F. Yang, Z. Wang, S. Chen, Y. Zhou, S. Zaman, B. Y. Xia, *Angew. Chem. Int. Ed.* **2020**, *59*, 10807–10813; *Angew. Chem.* **2020**, *132*, 10899–10905; g) L. Zhang, X.-X. Li, Z.-L. Lang, Y. Liu, J. Liu, L. Yuan, W.-Y. Lu, Y.-S. Xia, L.-Z. Dong, D.-Q. Yuan, Y.-Q. Lan, *J. Am. Chem. Soc.* **2021**, *143*, 3808–3816.

[7] a) N. Kornienko, Y. B. Zhao, C. S. Kley, C. H. Zhu, D. Kim, S. Lin, C. J. Chang, O. M. Yaghi, P. D. Yang, *J. Am. Chem. Soc.* **2015**, *137*, 14129–14135; b) J. X. Wu, S. Z. Hou, X. D. Zhang, M. Xu, H. F. Yang, P. S. Cao, Z. Y. Gu, *Chem. Sci.* **2019**, *10*, 2199–2205; c) D. Yang, S. Zuo, H. Yang, Y. Zhou, X. Wang, *Angew. Chem. Int. Ed.* **2020**, *59*, 18954–18959; *Angew. Chem.* **2020**, *132*, 19116–19121; d) Y. Guo, Y. Wang, Y. Shen, Z. Cai, Z. Li, J. Liu, J. Chen, C. Xiao, H. Liu, W. Lin, C. Wang, *J. Am. Chem. Soc.* **2020**, *142*, 21493–21501; e) J. Liu, D. Yang, Y. Zhou, G. Zhang, G. Xing, Y. Liu, Y. Ma, O. Terasaki, S. Yang, L. Chen, *Angew. Chem. Int. Ed.* **2021**, *60*, 14473–14479; *Angew. Chem.* **2021**, *133*, 14594–14600.

[8] a) T. Islamoglu, S. Goswami, Z. Li, A. J. Howarth, O. K. Farha, J. T. Hupp, *Acc. Chem. Res.* **2017**, *50*, 805–813; b) K. Manna, P. Ji, Z. Lin, F. X. Greene, A. Urban, N. C. Thacker, W. Lin, *Nat. Commun.* **2016**, *7*, 12610.

[9] a) F. Yang, W. Hu, C. Yang, M. Patrick, A. L. Cooksy, J. Zhang, J. A. Aguiar, C. Fang, Y. Zhou, Y. S. Meng, J. Huang, J. Gu, *Angew. Chem. Int. Ed.* **2020**, *59*, 4572–4580; *Angew. Chem.* **2020**, *132*, 4602–4610; b) J.-D. Yi, R. Xie, Z.-L. Xie, G.-L. Chai, T.-F. Liu, R.-P. Chen, Y.-B. Huang, R. Cao, *Angew. Chem. Int. Ed.* **2020**, *59*, 23641–23648; *Angew. Chem.* **2020**, *132*, 23849–23856; c) D.-H. Nam, O. Shekhah, G. Lee, A. Mallick, H. Jiang, F. Li, B. Chen, J. Wicks, M. Eddaoudi, E. H. Sargent, *J. Am. Chem. Soc.* **2020**, *142*, 21513–21521.

[10] Y. Bai, Y. Dou, L. H. Xie, W. Rutledge, J. R. Li, H. C. Zhou, *Chem. Soc. Rev.* **2016**, *45*, 2327–2367.

[11] a) J. Ma, A. G. Wong-Foy, A. J. Matzger, *Inorg. Chem.* **2015**, *54*, 4591–4593; b) L. Cao, Z. Lin, F. Peng, W. Wang, R. Huang, C. Wang, J. Yan, J. Liang, Z. Zhang, T. Zhang, L. Long, J. Sun, W. Lin, *Angew. Chem. Int. Ed.* **2016**, *55*, 4962–4966; *Angew. Chem.* **2016**, *128*, 5046–5050.

[12] G. C. Shearer, S. Chavan, S. Bordiga, S. Svelle, U. Olsbye, K. P. Lillerud, *Chem. Mater.* **2016**, *28*, 3749–3761.

[13] Y. Yang, L. Xing, W. Ren, D. Zhao, S. Jian, C. Cao, C. Wang, Y. Tian, X. Yu, X. Li, *Ind. Eng. Chem. Res.* **2019**, *58*, 22006–22014.

Manuscript received: December 14, 2021
Accepted manuscript online: December 28, 2021
Version of record online: January 17, 2022